The Astrophysical Journal, 729:145 (13pp), 2011 March 10 doi:10.1088/0004-637X/729/2/145

GAS AND DUST TOWARD DG Tau B AND VV CrA

Andrew J. Kruger[1], Matthew J. Richter[1], John S. Carr[2], Joan R. Najita[3], Greg W. Doppmann[3], and Andreas Seifahrt[1]
[1] Department of Physics, University of California at Davis, CA 95616, USA
[2] Remote Sensing Division, Naval Research Laboratory, Code 7210, Washington, DC 20375, USA
[3] National Optical Astronomy Observatory, Tucson, AZ 85719, USA
Received 2010 September 16; accepted 2011 January 8; published 2011 February 22

ABSTRACT

We present findings for DG Tau B and VV CrA, two of the objects observed in our *Spitzer* Infrared Spectrograph (IRS) project to search for molecular absorption in edge-on disks, along with near-IR spectroscopy of the CO fundamental transitions and mid-IR imaging. While the only gas absorption seen in the *Spitzer* IRS spectrum toward DG Tau B is CO_2, we use gas abundances and gas/ice ratios to argue that we are probing regions of the disk that have low organic molecule abundances. This implies that the rarity of detecting molecular absorption toward even edge-on disks with *Spitzer* IRS is a result of high dependence on the line of sight. We also argue that the disk around DG Tau B shows high amounts of grain growth and settling. For VV CrA, we use the silicate absorption feature to estimate a dust extinction, and model the disk with a spectral energy distribution fitting tool to give evidence in support of the disk geometry presented by Smith et al. where the primary disk is the main source of extinction toward the infrared companion.

Key words: circumstellar matter – ISM: abundances – protoplanetary disks – stars: individual (DG Tau B, VV CrA) – stars: pre-main sequence

1. INTRODUCTION

The study of disks of dust and gas surrounding young stars provides insight into the environment in which planets are likely to be forming. Molecular abundances in the disk can be used to understand the chemical evolution of the gas, disk processes such as radial and vertical mixing, and the effects of stellar irradiation on the disk chemistry (Bergin et al. 2007). While models predict disk chemistry in the Earth-like planet-forming regions (i.e., Markwick et al. 2002; Agúndez et al. 2008; Glassgold et al. 2009; Woods & Willacy 2009), supporting observations of the chemical tracers have been scarce to date.

The *Spitzer* Infrared Spectrograph (IRS) made observations that probed the chemistry of the inner disk, detecting molecular absorption (Lahuis et al. 2006) and emission (Carr & Najita 2008; Salyk et al. 2008). The resolution of IRS was well suited for detecting molecules with large equivalent widths from rovibrational *Q*-branches. Lahuis et al. (2006) detected warm C_2H_2, HCN, and CO_2 in absorption toward IRS 46, likely originating in the inner regions of a circumstellar disk seen near edge-on. Unfortunately, systems displaying molecular absorption are rare with, for example, IRS 46 being the only one of roughly 100 young stellar objects (YSOs) observed in the c2d Spitzer Legacy program (Evans et al. 2003).

Molecular C_2H_2 and HCN absorptions have also been detected toward GV Tau N (Doppmann et al. 2008; cf. Gibb et al. 2007), a classical infrared companion (IRC; Koresko et al. 1997). IRCs are binary companions to young stars that are faint in the visible but dominate the system flux in the infrared. Correia et al. (2007) found with MIDI/VLTI data that three IRCs, including GV Tau, are likely T Tauri stars (TTS) with the disk seen almost edge-on. Doppmann et al. (2008) found that the warm temperature and the relative velocity shifts of the molecular absorption further supported the edge-on disk model. Gibb et al. (2007) compared the molecular absorption abundances to predictions made by the chemical disk model of Markwick et al. (2002) and found them to be consistent with the inner region of a protoplanetary disk.

Because IRS 46 and GV Tau N show the rare features that are valuable for probing the inner disk chemistry, it is advantageous to study more disks with similar attributes. We were granted time with *Spitzer* IRS to obtain high signal-to-noise (S/N) spectra of seven YSOs. Our target selection was limited to systems thought to be similar to IRS 46 and GV Tau N with a large column of gas between the observer and the emitting source necessary for absorption studies: three circumstellar disks seen near edge-on and four classical IRCs. DG Tau B and VV CrA are two of the objects observed in this project.

Mundt & Fried (1983) first designated DG Tau B as the source of a Herbig–Haro jet (HH 159) that flows 15° to the plane of the sky. Near-IR *Hubble Space Telescope* (*HST*) images show DG Tau B to be a bipolar reflection nebula embedded in an envelope (Stapelfeldt et al. 1997). Stark et al. (2006) modeled near-IR disk images, finding that it likely has a disk inclination of ∼73°. Previous *Spitzer* IRS measurements have shown that this system displays CO_2 ice (Watson et al. 2004) and gas absorption (Pontoppidan et al. 2008), so we obtained higher S/N to search for other species.

The northeast component of the VV CrA system is a classical IRC, and Correia et al. (2007) used MIDI/VLTI observations to show that the IRC is likely a TTS seen near edge-on. Smith et al. (2009, hereafter S09) used CRIRES/Very Large Telescope (VLT) to detect CO gas absorption with multiple temperature components toward the primary and IRC. They proposed two disk morphology scenarios to explain the CO absorption seen toward VV CrA IRC: (A) the gas absorption is in a disk around the primary in the line of sight to the IRC and (B) all the CO absorption is in a disk around the IRC. While S09 consider Case A to be more likely, with the observed CO residing in the warm surface layer and cooler midplane of the primary disk, neither case could be dismissed so we consider both geometries.

In addition to the IRS spectra, we observed both targets with ground-based telescopes. We used *M*-band spectroscopy to observe the CO fundamental ($\Delta v = 1$) transitions toward both objects. Observing these lines probes a wide range of radii in circumstellar disks and has proven useful for exploring

the disk gas in the inner disk regions (Najita et al. 2003; Brittain et al. 2007, and references therein). Finally, because molecular absorption is limited to studies in the line of sight to the continuum-emitting source and the *Spitzer* IRS spectrum combines both VV CrA components, we obtained mid-IR images of VV CrA in order to map the continuum at spatial scales unavailable with *Spitzer* and to separate the continuum flux for the two components.

We present here results for DG Tau B and VV CrA from our study of sources in the *Spitzer* survey. We include high-resolution absorption spectroscopy and, for VV CrA, mid-IR imaging. In Section 2, we introduce the observations taken; in Section 3, we describe the data reduction and discuss the molecular detections; and we discuss modeling and the conclusions in Section 4.

2. OBSERVATIONS

2.1. Spitzer IRS

We observed DG Tau B and VV CrA as part of our Cycle 5 General Observers project, Program ID 50152. We used the *Spitzer* IRS (Houck et al. 2004) short-low (SL) and short-high (SH) modules in stare mode to search for molecular absorption species with large equivalent widths such as rovibrational *Q*-branches. The SL spectra obtained have a coverage of 5.2–14.5 μm with $R = \lambda/\Delta\lambda = 60$–127, and the SH spectra have a coverage of 9.9–19.6 μm with $R = 600$. We adopted the observing technique described in Carr & Najita (2008). In order to verify the repeatability of the observations, we lowered the exposure time for each data frame and increased the number of integrations. Each setting (SL1, SL2, SH) thus had 12 on-source data frames at each nod position, each with a 6 s integration. For hot pixel subtraction and to remove background emission, each observation was supplemented by off-source integrations for half the time as on-source (Carr & Najita 2008). DG Tau B (AOR: 25680128) was observed on 2008 November 5 at $4^h27^m2\overset{s}{.}66$ + 26°5′30″.5 (J2000). VV CrA (AOR: 25680896) was observed on 2008 November 18 with the pointing on the IRC at $19^h3^m6\overset{s}{.}86-37°12'48''.2$ (J2000). The coordinates for VV CrA were chosen to center the slit on the IRC, and were calculated using a 2″.1 offset, 44° east of north (Chelli et al. 1995) from the known primary coordinates found on SIMBAD. Both observations used the nominal pointing accuracy of 0″.1.

2.2. Infrared Spectroscopy

On 2008 November 16, we used NIRSPEC (McLean et al. 1998) on Keck II in echelle mode with $R = 25{,}000$ to detect the CO fundamental transitions toward DG Tau B. Our instrument setup included the *M*-wide blocking filter, along with echelle and cross-disperser settings to image orders 14–16 so we could view the ^{12}CO $v = 0$–1 $R(0)$–$R(9)$ and $P(25)$–$P(30)$ transitions. We used the standard ABBA nod sequence with thirty 1 s exposures co-added at each position. Standard star observations were taken before and after DG Tau B for telluric division.

For a similar observation of both VV CrA components, we used Phoenix (Hinkle et al. 1998) on Gemini South on 2009 April 6. We used the standard four pixel slit (0″.35), giving $R = 50{,}000$. The M2150 filter and instrument settings were used to detect the ^{12}CO $v = 1$–0 $R(3)$–$R(5)$ transitions near 4.66 μm. Each ABBA nod position had a 120 s integration (four 30 s exposures co-added internally), and we used a telescope position angle of 44° to place both binary components within the slit. Standard star observations were taken after the science frames for telluric division.

2.3. Imaging

We imaged the binary components using T-ReCS (Telesco et al. 1998) on Gemini South using six filters ranging from 7.7 to 25.5 μm (see Table 1). We cycled through each of the filters while staying on the science target, and took calibration images of standard stars before and after the science target for point-spread function (PSF) corrections and to test for any changes in PSF or calibration during the target observation. Observations were conducted using the standard chop-nod mode. When we nodded, the target was placed at the center of the field of view for half the total integration time, and the other half placed the target into a corner of the array for frames to be used for background subtraction.

3. DATA REDUCTION AND DETECTIONS

3.1. Spitzer IRS

We used the reduction technique described in Carr & Najita (2008). We used the integrations of the nearby blank sky to identify hot pixels, which were removed from the science frames by interpolation using custom routines in IDL. We then used IRAF to extract the raw spectra from each individual raw data frame. A similar procedure was used to extract spectra from the regularly observed HR 6688, which we used for standard star division, to remove fringing, and for flux calibration. Because the fringing in each observation is dependent on the target position on the slit, each data frame was divided by the standard star observation that showed the least amount of fringing in the shorter wavelengths after division. Any residual fringing was removed using IRSFRINGE in IDL. Calibration of the SL spectra is highly dependent on the slit position, so we used the optimal point source extraction in the *Spitzer* IRS Custom Extractor (SPICE; version 2.2) to extract the individual spectra before co-adding.

The *Spitzer* IRS spectrum of DG Tau B, with an average S/N = 100 per pixel, can be seen in Figure 1. A 10% continuum flux difference between the SH and SL modules was corrected by scaling the SH by a constant, without any adjustment to the continuum shape, to match the SL at wavelengths where the orders overlap. The spectrum shows the amorphous silicates, CO_2 ice absorption, water ice, and an absorption feature at 6.8 μm, which is possibly due to methanol (Watson et al. 2004; Zasowski et al. 2009), as well as the CO_2 gas absorption at 15.2 μm as previously recognized by Pontoppidan et al. (2008). We further detect [Ne II] emission at 12.81 μm with line intensity $(3.0 \pm 1.5) \times 10^{-15}$ erg cm^{-2} s^{-1}.

The *Spitzer* IRS spectrum of VV CrA shown in Figure 1, with S/N = 160 per pixel, is of the combined binary components as they were unresolved within the slit. It can be seen that there is a continuum mismatch between SH and SL modules, likely due to being centered on the IRC and from the modules having different slit position angles and widths. The SH and SL modules have position angles 221°.5 and 136°.7 (for a *Spitzer* roll angle of 0°), respectively, so during the SH observation the binary components were separated 0″.31 across the 4″.7 slit, while during the SL observation the components were separated 1″.20 across the 3″.6 slit. The SL1 is at an intermediate wavelength and flux, so we scaled the SL2 and SH modules by a constant to match the intermediate SL1 continuum. We find that the system displays amorphous silicate absorption and CO_2 ice absorption at 15.2 μm.

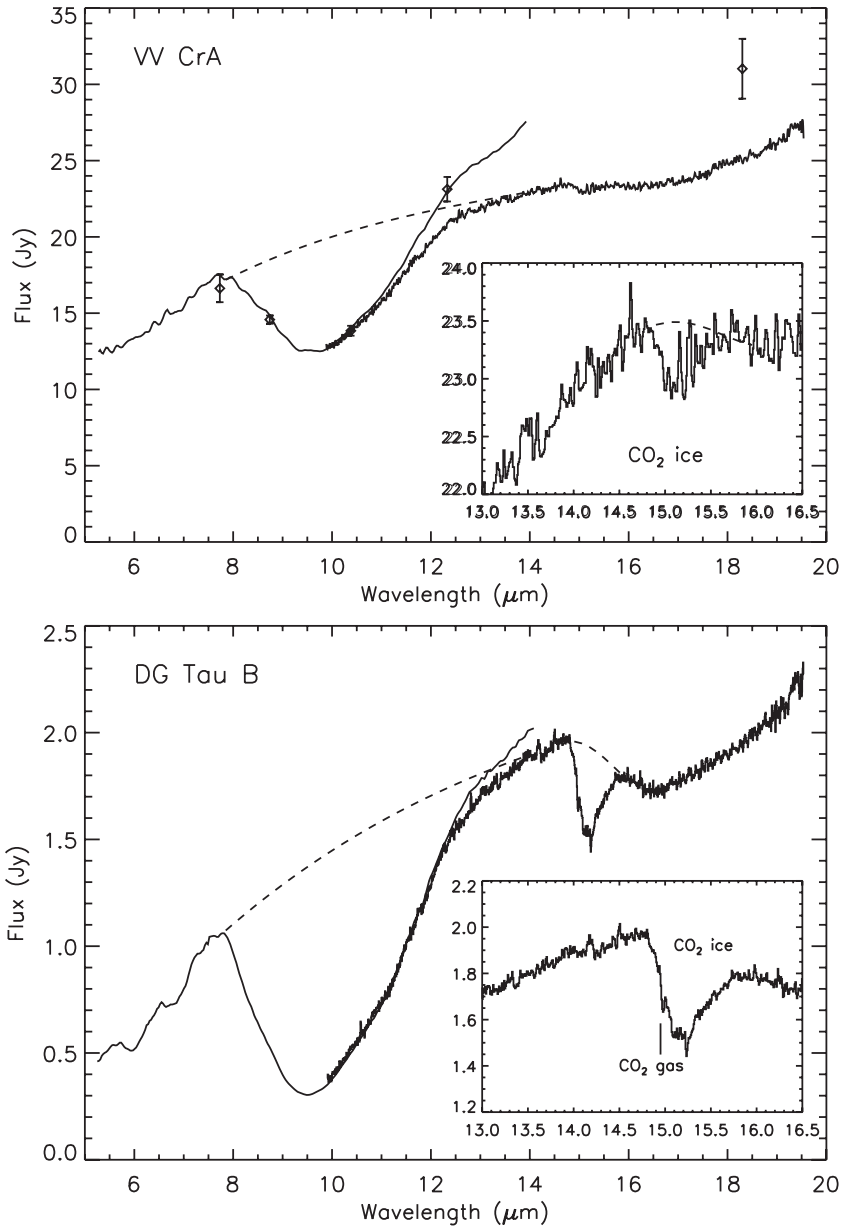

Figure 1. *Spitzer* IRS spectra of DG Tau B and VV CrA. DG Tau B displays water (6 μm) and "methanol" (6.8 μm) ice absorption; both targets show amorphous silicates (8–12 and 15–19 μm) and CO_2 ice (15.2 μm) absorption. Overplotted are the continua used to find the silicate and CO_2 ice peak optical depths (dashed lines; see the text). The VV CRA spectrum also shows the summed fluxes of the binary components as found with T-ReCS (diamonds), with each point summing 70% of the primary flux and 100% of the IRC flux.

3.2. CO Fundamental

To reduce our Phoenix and NIRSPEC spectra, we used standard spectral reduction routines in IRAF. After flat-fielding each frame, we subtracted nod pairs to remove the sky emission. The target spectra were extracted using *apall* in IRAF with background subtraction using both sides of the profile (from both sides of the total binary profile for VV CrA). In order to increase S/N and for better telluric division, we first extracted the spectrum from each individual science and standard star frame (standards listed in Table 1). We then divided each science spectrum by each standard star spectrum using their corresponding airmass, then co-added the spectra. We found that applying telluric division before co-adding the spectra resulted in better telluric correction. The wavelength solution was made by using the IRAF task *identify* on sky emission lines in co-added science frames. The rest-frame wavelengths of the emission lines were taken from the HITRAN database (Rothman et al. 1998).

Our NIRSPEC spectra of DG Tau B, seen in Figure 2, have S/N = 21 and 28 per pixel for orders 15 and 16, respectively, and we found both ^{12}CO and ^{13}CO in absorption (see Table 2). The average line profiles for the low- and high-J ^{12}CO transitions have slightly different velocity shifts and widths (see Table 3 and Figure 3) which indicates that we are likely probing multiple velocity components.

We were able to clearly resolve the VV CrA components with Phoenix, and the spectra, shown in Figure 4, had an average S/N of 220 per pixel for the IRC and 280 for the primary. The VV CrA IRC displays ^{13}CO and optically thick ^{12}CO in absorption (see Table 4), as well as a shallow, broad ^{12}CO absorption feature with $V_{\rm LSR} = -24\,{\rm km\,s^{-1}}$ and FWHM $= 32.9\,{\rm km\,s^{-1}}$ (see line

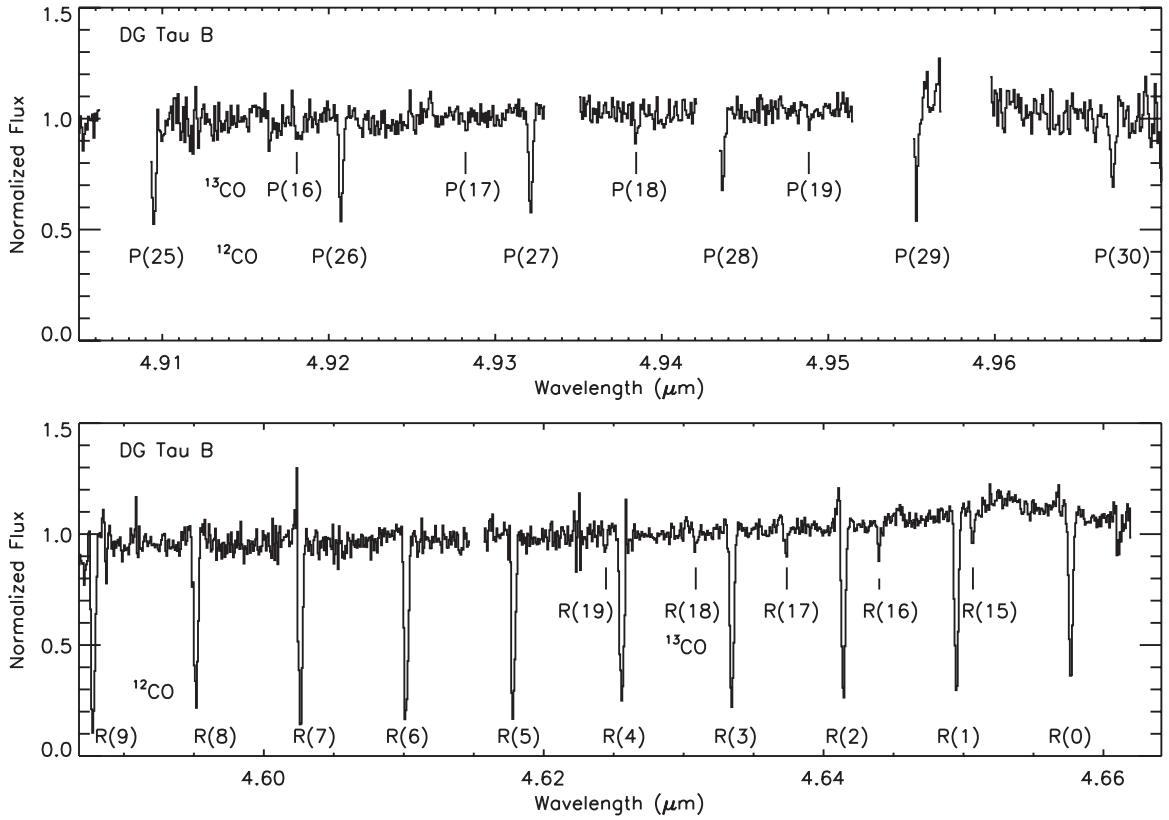

Figure 2. CO fundamental absorption spectra for DG Tau B in orders 15 (above) and 16 (below) with detected transitions marked.

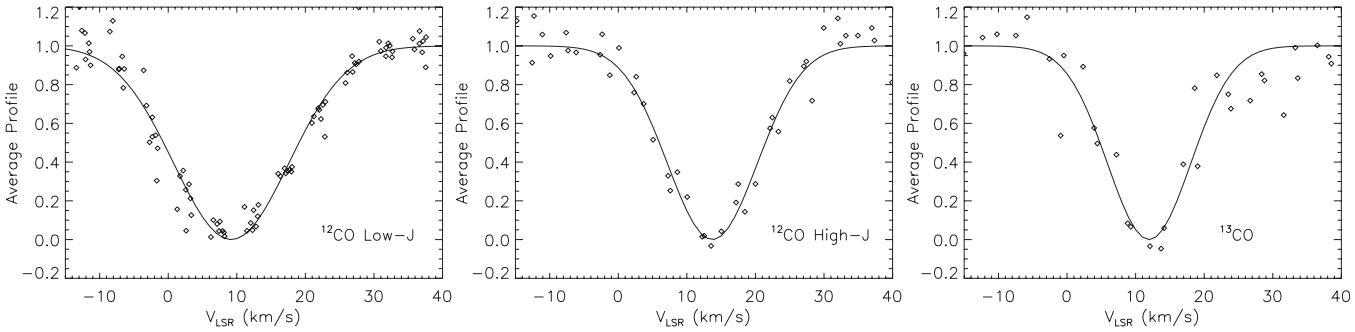

Figure 3. ^{12}CO and ^{13}CO line profiles for DG Tau B. It can be seen that the ^{12}CO low-J R(0–7) transitions (left) have a different profile from the ^{12}CO high-J P(25–27, 30) (middle) and ^{13}CO R(15–17) transitions (right).

Table 1
Detailed List of Observations Taken for this Work

Target	Date	Instrument	Mode	Setting	Total Int. Time (s)	Standard Star
VV CrA	2008 Nov 18	*Spitzer* IRS	Spectrum	SL1, SL2	151	
				SH	151	HR 6688
	2009 Apr 6	Phoenix	Spectrum	4.66 μm	1920	HD 209952
	2009 Jun 8	T-ReCS	Image	Si-1, 7.37 μm	319	HD 181109
				Si-2, 8.74 μm	203	HD 181109
				Si-4, 10.38 μm	203	HD 181109
				Si-6, 12.33 μm	203	HD 181109
				Qa, 18.3 μm	261	HD 196171
				Qb, 24.56 μm	319	HD 196171
DG Tau B	2008 Nov 5	*Spitzer* IRS	Spectrum	SL1, SL2	151	
				SH	151	HR 6688
	2008 Nov 16	NIRSPEC	Spectrum	4.6 and 4.9 μm	3360	HR 1641

profile in Figure 5). The VV CrA primary shows cold ^{12}CO within broader ^{12}CO emission lines. The cold, unresolved ^{12}CO absorption lines have FWHM $= 5.35\,\mathrm{km\,s^{-1}}$ while using the four-pixel slit width with resolution $R = 6\,\mathrm{km\,s^{-1}}$, suggesting

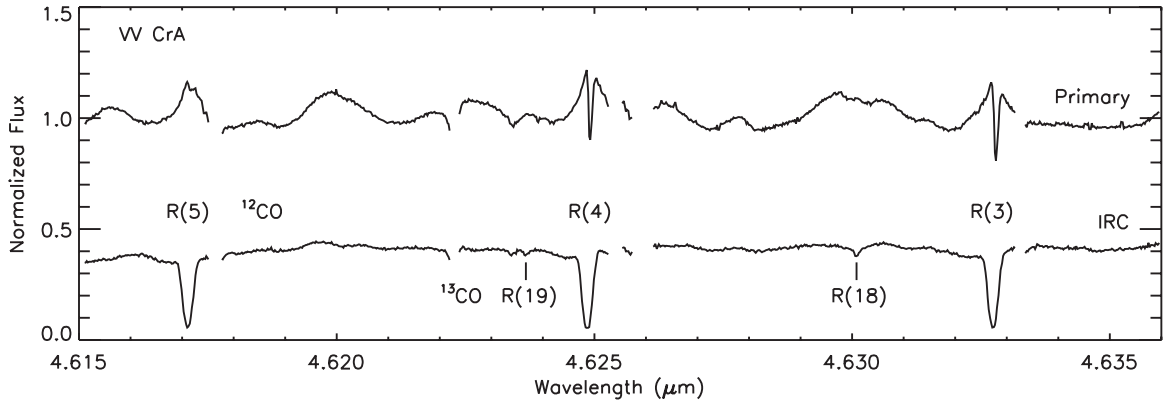

Figure 4. CO fundamental absorption spectra for the VV CrA binary components with detected transitions marked. The primary (upper spectrum) and IRC (lower spectrum) are normalized by the primary flux.

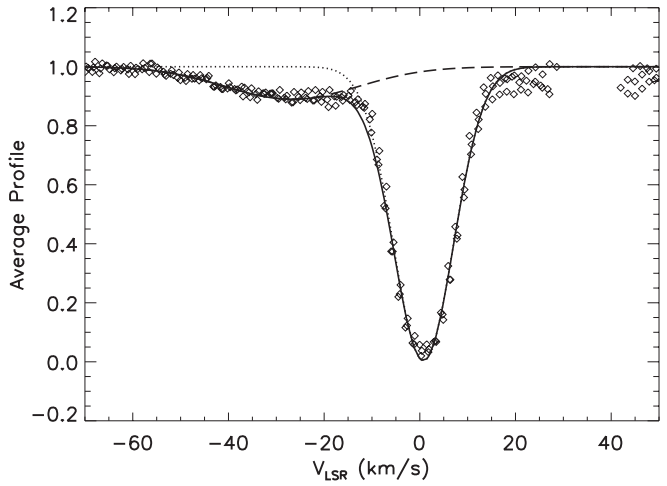

Figure 5. ^{12}CO line profile for the VV CrA IRC showing optically thick, low-J transitions (dotted line; $V_{\rm LSR} = 0.78\,{\rm km\,s^{-1}}$, FWHM $= 14.8\,{\rm km\,s^{-1}}$) and a broad, optically thin line (dashed line; $V_{\rm LSR} = -24\,{\rm km\,s^{-1}}$, FWHM $= 32.9\,{\rm km\,s^{-1}}$). The solid line is the combined fit.

our resolution was limited by the PSF of the target rather than the entire slit width.

The primary and IRC both also show a complicated emission structure. This structure can be understood as a blend of broad CO emission lines from numerous rovibrational levels. Both of the VV CrA components show CO overtone emission (Prato et al. 2003) with emission up to at least the $v = 4$–2 vibrational band. The observed CO fundamental bands are consistent with the expectation of a hot, optically thick emission spectrum. In this respect, the spectra are similar to the extreme TTS RW Aur (Najita et al. 2003).

3.3. Imaging

The T-ReCS images show a resolved VV CrA binary (Figure 6). Images were made by subtracting nod pairs and co-adding the resulting images. High winds caused poor image quality, so we created custom IDL routines to center each data frame on the peak of the primary companion before co-adding. This gave better final image quality, but we did not detect any extended emission. We measured photometric fluxes using a 2.″1 aperture centered on each component and on the standard star observations, which were then used for flux calibration (see results in Table 5). While the primary does show a hint of silicate absorption, a majority of this feature seen in the *Spitzer* IRS spectrum originates in the IRC. We find that the broadband fluxes measured with T-ReCS fit the *Spitzer* IRS spectrum if we assume that we are collecting only 70% of the flux from the primary (see Figure 1), with the flux loss likely due to slit losses from being centered on the IRC.

Table 2
Measured Equivalent Widths and Doppler Shifts of the CO Fundamental Absorption Lines Used in Measuring Column Density and Temperatures for DG Tau B

Line ID	Equivalent Width ($\rm cm^{-1}$)	Doppler Shift ($V_{\rm LSR}$, $\rm km\,s^{-1}$)
^{12}CO $P(25)$	0.0458 ± 0.003	14.7 ± 1.3
^{12}CO $P(26)$	0.0451 ± 0.002	13.2 ± 0.6
^{12}CO $P(27)$	0.0423 ± 0.002	13.1 ± 0.6
^{12}CO $P(30)$	0.0282 ± 0.001	13.9 ± 0.8
^{12}CO $R(0)$	0.111 ± 0.003	9.5 ± 0.3
^{12}CO $R(1)$	0.120 ± 0.004	9.7 ± 0.3
^{12}CO $R(2)$	0.117 ± 0.004	9.6 ± 0.3
^{12}CO $R(3)$	0.118 ± 0.004	8.8 ± 0.3
^{12}CO $R(5)$	0.125 ± 0.01	8.9 ± 0.5
^{12}CO $R(6)$	0.127 ± 0.007	8.6 ± 0.4
^{12}CO $R(7)$	0.134 ± 0.007	9.6 ± 0.4
^{12}CO $R(8)$	0.114 ± 0.005	8.1 ± 0.4
^{12}CO $R(9)$	0.136 ± 0.009	8.3 ± 0.5
^{13}CO $R(15)$	0.0175 ± 0.0006	12.8 ± 1.0
^{13}CO $R(16)$	0.0180 ± 0.0006	12.3 ± 0.7
^{13}CO $R(17)$	0.0133 ± 0.005	10.7 ± 1.1
^{13}CO $R(18)$	0.0079 ± 0.0003	14.0 ± 2.2
^{13}CO $R(19)$	0.0091 ± 0.0004	10.6 ± 2.2

4. DISCUSSION

4.1. Molecular Detections

4.1.1. DG Tau B

All of our models of the CO and CO_2 gas were done using a single temperature slab model. We fit the ^{13}CO R(16–19) transitions with the assumption that the transitions are optically thin and found a temperature of 288±7 K with column density of $N(^{13}{\rm CO}) = (3.5 \pm 0.6) \times 10^{17}{\rm cm^{-2}}$ (see population diagram in Figure 7). If we fit the high-J ^{12}CO P(25–27, 30) lines to an optically thin model as well, we find that the gas would be at a high temperature of 930 ± 60 K with $N(^{12}{\rm CO}) = (7.86 \pm 0.2) \times 10^{17}\,{\rm cm^{-2}}$. However, this would indicate a ^{12}CO/^{13}CO ratio of only 2.2, much lower than the mean ratio found in the local interstellar medium (ISM; Wilson 1999). This indicates

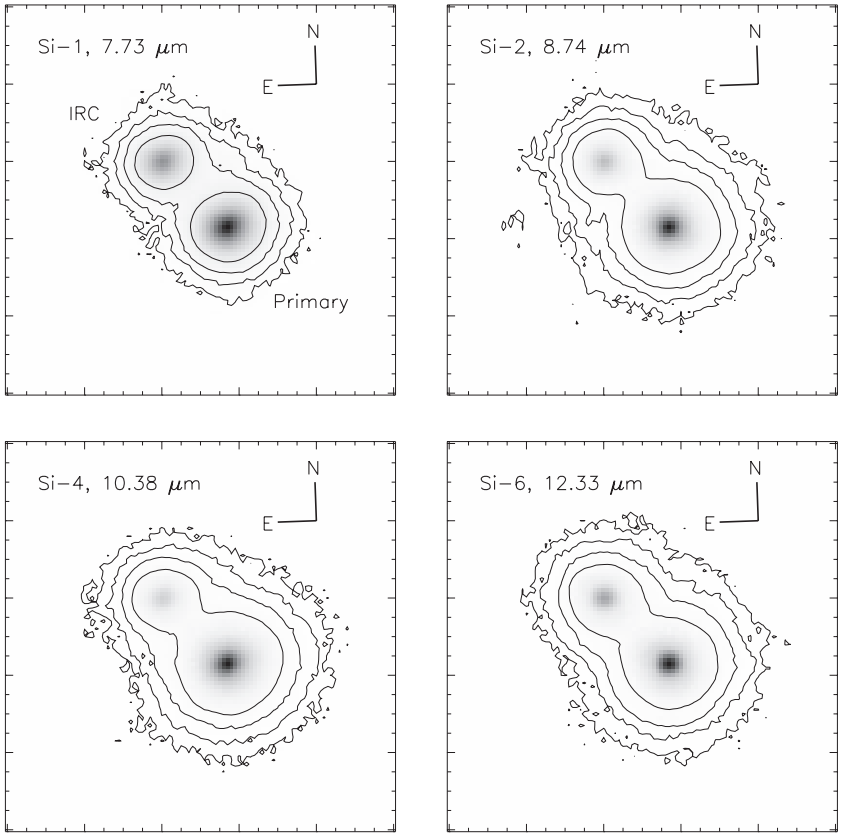

Figure 6. Images of VV CrA taken with T-ReCS in the Si-1 (7.73 μm), Si-2 (8.74 μm), Si-4 (10.38 μm), and Si-6 (12.33 μm) filters with the IRC being the NE component. The contours are drawn at 5σ, 10σ, 20σ, and 50σ. The 5σ contours, in Jy pixel^{-1}, correspond to $5\sigma_{\rm Si-1} = 0.080$, $5\sigma_{\rm Si-2} = 0.020$, $5\sigma_{\rm Si-4} = 0.023$, and $5\sigma_{\rm Si-6} = 0.038$.

Table 3
Measured Parameters for Molecular Absorption Toward DG Tau B and VV CrA

Target	Molecule	T (K)	N (10^{17} cm^{-2})	$V_{\rm LSR}$ (km s^{-1})	FWHM (km s^{-1})[a]
DG Tau B	High-J ^{12}CO[b]	370 ± 20	240 ± 20	13.4 ± 0.4	13.7 ± 0.4
	Low-J ^{12}CO	...	...	9.3 ± 0.6	20.0 ± 0.4
	^{13}CO	288 ± 7	$3.50 \pm .06$	12.0 ± 0.5	14.3 ± 0.4
	CO_2	300	0.29	...	2.1[c]
VV CrA primary	^{12}CO	29 ± 4	0.026 ± 0.004	4.88 ± 0.4	5.35 ± 0.2
VV CrA IRC	^{12}CO	...	...	0.78 ± 0.05	14.8 ± 0.2
	^{13}CO	...	...	1.75 ± 0.3	10.2 ± 0.8

Notes.
[a] Line widths are of convolved spectra.
[b] Assuming ^{12}CO/^{13}CO abundance ratio of 69 ± 6 (Wilson 1999).
[c] Doppler b-value; see the text.

that all of the observed ^{12}CO lines are likely optically thick. To constrain the temperature of the absorbing gas, we modeled ^{12}CO gas with a column density of 2.42×10^{19} cm^{-2}, estimated using the $N(^{13}\mathrm{CO})$ and mean isotopic ratio of 69 ± 6 from Wilson (1999), and varied the turbulence and temperature. We could not model all the ^{12}CO transitions to a single temperature, with the low-J transitions always showing higher optical depths than permitted by fits to the high-J transitions. This is likely due to multiple velocity components being viewed in the low-J transitions, which would account for the difference in velocity shift and width from the high-J transitions. We thus fit only the high-J P(25–27, 30) transitions, and the goodness of fit, shown in Figure 7, indicates that the gas is likely 370 ± 20 K with a Doppler b-value $V_{\rm turb} = 2.1 \pm 0.2$ km s^{-1}. If the ^{12}CO is self-shielding and the ^{12}CO/^{13}CO is raised to 100, similar to the ratios found in S09, these values would not change much as the temperature would still be ~350 K and $V_{\rm turb} \sim 2$ km s^{-1}.

We find that the model for the CO_2 gas has degenerate fits by changing the microturbulence and temperature, so we use the Doppler b-value of 2.1 km s^{-1} found with the CO gas, and find $T = 300$ K and $N(CO_2) = 2.9 \times 10^{16}$ cm^{-2}. We further find upper limits for C_2H_2 and HCN, two other organic molecules detected toward IRS 46 (Lahuis et al. 2006), to compare molecular abundance ratios. To get upper limits on column densities, we note that temperatures of both the CO and CO_2 gases toward DG Tau B are similar to that found toward IRS 46 (400 and 300 K, respectively); thus, we start with the assumption that if C_2H_2 and HCN are present, they would have similar temperatures to IRS 46 (700 and 400 K, respectively). To derive the upper limits, we individually modeled the absorption

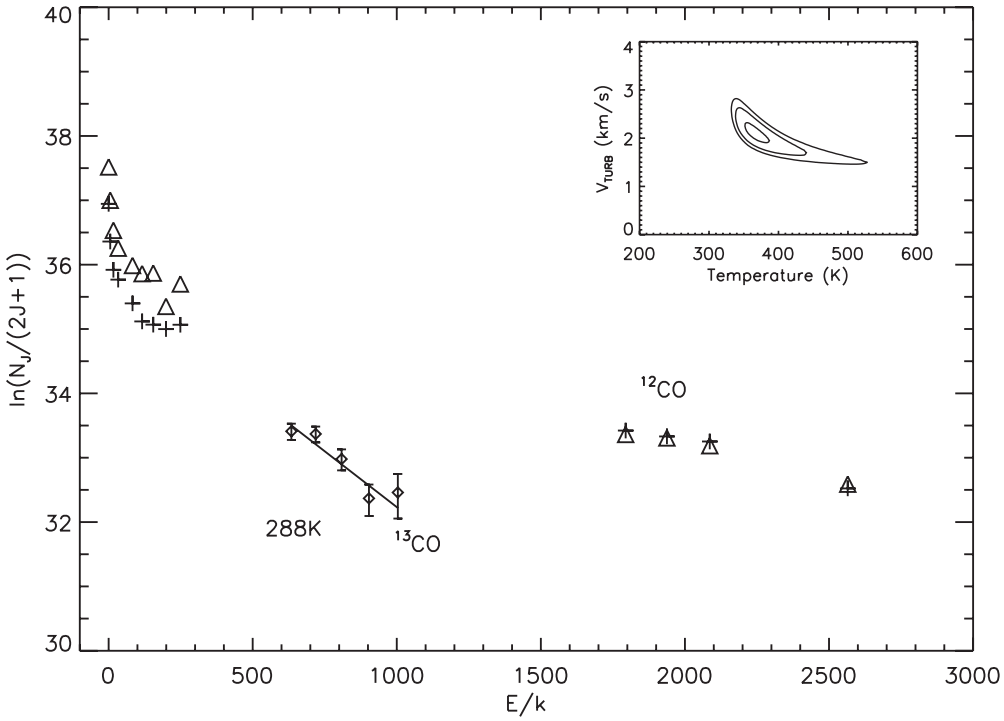

Figure 7. Population diagram of ^{12}CO and ^{13}CO absorption as seen toward DG Tau B. The ^{13}CO (diamonds) is modeled as being optically thin with temperature 288 K. The ^{12}CO line transitions are optically thick (shown with triangles, indicating these are lower limits) and we model the gas (crosses) with the column density of $N(^{12}\mathrm{CO}) = 2.42 \times 10^{19}$ cm^{-2}, $T = 365$ K, and $V_{\mathrm{turb}} = 2.1$ km s^{-1}. Inset: goodness-of-fit contours for the temperature and turbulence velocity of the ^{12}CO P(25–27, 30) absorption lines seen toward DG Tau B assuming a column density of 2.42×10^{19} cm^{-2}. The contours show the 68%, 95%, and 99% confidence levels.

Table 4
Measured Equivalent Widths and Doppler Shifts of the CO Fundamental Absorption Lines for VV CrA

Target	Line ID	Equivalent Width (cm^{-1})	Doppler Shift (V_{LSR}, km s^{-1})
IRC	^{12}CO R(3)	0.102 ± 0.01	1.1 ± 0.1
	^{12}CO R(4)	0.105 ± 0.02	0.3 ± 0.1
	^{12}CO R(5)	0.099 ± 0.005	0.8 ± 0.06
	^{13}CO R(18)	0.0106 ± 0.0008	1.6 ± 0.4
	^{13}CO R(19)	0.0055 ± 0.0004	1.8 ± 0.3
Primary	^{12}CO R(3)	0.0127 ± 0.0005	5.2 ± 0.1
	^{12}CO R(4)	0.0115 ± 0.0004	4.5 ± 0.1
	^{12}CO R(5)	0.0013 ± 0.00005	5.4 ± 0.4

Table 5
Fluxes for the VV CrA Primary and IRC as Measured with T-ReCS Imaging

Filter	Primary	IRC
	Flux (Jy)	Flux (Jy)
Si-1, 7.73 μm	13.7 ± 0.7	7.0 ± 0.4
Si-2, 8.74 μm	14.4 ± 0.2	4.5 ± 0.1
Si-4, 10.38 μm	15.0 ± 0.3	3.3 ± 0.1
Si-6, 12.33 μm	20.5 ± 0.7	8.7 ± 0.3
Qa, 18.3 μm	28.4 ± 1.6	11.1 ± 0.8
Qb, 24.56 μm	35.0 ± 17.8	25.1 ± 13.5

spectrum for the molecules at those temperatures. We then used the model-generated profiles to measure feature strengths at various wavelengths in the DG Tau B spectrum, giving us a distribution of feature strengths that we would expect to measure given only the spectral noise. We then set the upper limit as the column density that would provide a 3σ integrated intensity. We find that the upper limit on the C_2H_2/CO_2 ratio (<0.19) is not very different from the ratio measured for IRS 46 (0.3), suggesting that the non-detection of C_2H_2 in our data may be the result of the lower absorbing column in this source. The upper limit on the HCN/CO_2 ratio (<0.22) is a factor of two smaller than that measured for IRS 46 (0.5). Modeling the gas at higher temperatures with similar column densities decreases the integrated intensity of the absorption features, so higher gas temperatures would result in higher upper limits on the column densities. A temperature increase of 50 K would raise the column density upper limit by ∼15% for both molecules. If we model the molecules at 300 K, like the CO_2 gas, the upper limits of the C_2H_2/CO_2 and HCN/CO_2 ratios would be 0.06 and 0.18, respectively.

The [Ne II] emission, as seen toward DG Tau B, is a feature commonly found by *Spitzer* IRS toward TTSs (Lahuis et al. 2007). Güdel et al. (2010) showed that among TTSs, the [Ne II] emission strength increases with the jet mass loss rate, the latter as inferred from the high-velocity component of the [O I] emission. Mundt & Fried (1983) found that HH 159, a jet associated with DG Tau B, has a mass-loss rate of 10^{-9} $M_\odot$ yr^{-1}. If we assume that DG Tau B is 145 pc away, our measured [Ne II] luminosity of 7.5×10^{27} erg s^{-1} is similar to that of TTSs with comparable mass-loss rates (cf. Figure 5; Güdel et al. 2010).

As we do not see C_2H_2 and HCN in the disk, a simple explanation is that they have low abundances in the disk. This could possibly be due to photodissociation. The [Ne II] emission may be an indication that the gas is irradiated by X-rays (Glassgold et al. 2007), and/or UV irradiation (Hollenbach & Gorti 2009), which in turn could reduce the C_2H_2 and HCN in the disk. However, many TTSs with [Ne II] emission similar to or stronger than that of DG Tau B show emission in C_2H_2 and HCN (J. S. Carr & J. R. Najita 2011, in preparation).

Table 6
Measured Column Densities and Ratios for DG Tau B Compared to IRS 46 (Lahuis et al. 2006)

Abundance Ratios	DG Tau B	IRS 46
N(CO) (10^{18} cm^{-2})	24.2[a]	2
N(HCN)/N(CO)	<0.00026	0.025
$N(C_2H_2)/N$(CO)	<0.00023	0.015
$N(CO_2$ gas)/N(CO)	0.0012	0.05
$N(CO_2$ ice)/N(CO)[b]	0.022	0.12
$\tau_{SiO}/\tau_{CO_2 ice}$	6.6	8.6

Notes.
[a] Using ^{13}CO column density and isotopic ratio in local ISM, see the text.
[b] CO_2 ice column densities are taken from Pontoppidan et al. (2008).

Alternatively, as C_2H_2 and HCN are commonly found in circumstellar disks (Pontoppidan et al. 2010), these species could be in the disk, but simply not in our line of sight. This may be implied by the most striking difference between DG Tau B and IRS 46: while the column density of CO toward DG Tau B is only 10 times that toward IRS 46, the gas ratios to CO in DG Tau B are 1%–2% of that found toward IRS 46 (see Table 6). Also, the limits on the ratios $N(C_2H_2)/N$(CO) and N(HCN)/N(CO) are much smaller for DG Tau B than the measured ratios toward GV Tau N (Gibb et al. 2007). While the large CO column toward DG Tau B implies that we are probing a large amount of disk material, we are not detecting the large columns of other gaseous species.

The disk chemistry model in Agúndez et al. (2008) may provide further insight into the disk conditions probed by our observations. They focus their models on the photon dominated region of the disk, and use photochemistry to estimate the steady state abundances of simple organic molecules. They show that the C_2H_2 and HCN have low abundances for disk radii >1.5 AU, and the CO/CO_2 is large for radii <1 AU. While the temperatures we measured for CO and CO_2 are cooler than expected for radii <1 AU, the vertical structure of these molecules is not available. One possible scenario is that the line of sight passes below the main temperature inversion layer.

Doppmann et al. (2008) note GV Tau N has a larger $\tau_{SiO}/\tau_{CO_2 ice}$ than other Class I YSOs in Taurus (typically $\leqslant 4$; Furlan et al. 2008), and suggest this could happen if a majority of the probed silicate is residing in a warm region of the disk atmosphere. We calculate this ratio for DG Tau B and IRS 46 for comparison. To do this, we used a polynomial fit across the features to determine the initial continua. For the silicate feature, we fit to the continuum in the 13–14.8 μm region, and to the continuum between the water and "methanol" ice at wavelengths <7.8 μm. For the CO_2 feature, we assume the CO_2 ice is located at larger disk radii than the silicate, as found by Watson et al. (2004), so the ice is absorbing from a continuum already including the silicate absorption features. We thus use a continuum for DG Tau B that is modified from that used in Watson et al. (2004), found by fitting the spectrum at wavelengths 13–14.8 μm and >15.6 μm. The continuum fits are shown in Figure 1. We then used the relation $I_{obs} = I_{em}\exp(-\tau)$, where I_{obs} is the observed flux and I_{em} is the emitted continuum, to find $\tau_{SiO} = 1.52 \pm 0.06$ and $\tau_{CO_2} = 0.24 \pm 0.01$. Lahuis et al. (2006) found IRS 46 to have $\tau_{SiO} = 0.86$, and Pontoppidan et al. (2008) show $\tau_{CO_2} = 0.1$. While both IRS 46 and DG Tau B have higher ratios than found for Class I objects in Taurus, both GV Tau N and IRS 46 have higher ratios (~9 and 8.6, respectively) than DG Tau B (6.6 ± 0.4). Additionally, using the CO_2 ice column density measurements for IRS 46 and DG Tau B found in Pontoppidan et al. (2008), we find that IRS 46 has a higher CO_2 gas/ice ratio, about eight times than that of DG Tau B. This suggests that the line of sight toward IRS 46 is predominantly probing warmer regions than that toward DG Tau B, resulting in the detection of C_2H_2 and HCN.

Alternatively (or in addition), the ratios of CO_2 gas, ice, and silicate could simply be a factor of disk inclination. If the lines of sight for IRS 46 and GV Tau N pass higher in the disk atmosphere than that for DG Tau B, raising the silicate to ice ratio, it could also be probing a moderately different region of the disk where the organic molecules reside. If we are only viewing the cold to moderate temperature (<400 K) regions deeper in the disk in DG Tau B, the C_2H_2 and HCN production would be lower in these regions, thus lowering the steady state abundances (Agúndez et al. 2008) and resulting in their non-detection. If this is the case, the detection of pre-biotic molecules in absorption may be highly sensitive to the line of sight, even for edge-on disks. This could possibly further explain the rarity of molecular absorption among *Spitzer* IRS spectra of young stars.

4.1.2. VV CrA

Our Phoenix spectra of the VV CrA system show ^{12}CO transitions in absorption toward both components. However, the optically thick lines for the IRC and few lines for the primary make it difficult to extract accurate temperature and column density measurements. We therefore use the CO abundances reported in S09 for the IRC. To get the temperature and column density of the cold ^{12}CO toward the primary, we obtained the CRIRES spectra used in S09 from the ESO archive. We reduced the data using a similar procedure to that used for Phoenix and NIRSPEC, although the wavelength calibration and telluric division were performed using a telluric model fitter (Seifahrt et al. 2010). We find that the cold gas toward the primary has a column density of $(2.6 \pm 0.4) \times 10^{15}$ cm^{-2} and temperature 29 ± 4 K (population diagram is shown in Figure 8). While Doppler velocity shifts of the ^{12}CO $v = (2–0)$ absorption lines reported for the IRC in S09 are ~3–5 km s^{-1}, the CRIRES spectrum shows a smaller shift for the $v = (1–0)$ lines (~1 km s^{-1}), similar to the shift we found with the Phoenix spectrum (0.78 ± 0.5 km s^{-1}). One change between the Phoenix and CRIRES spectra is that the CRIRES spectrum does not show the broad, shallow lines, but rather displays other ^{12}CO lines in the -40 to -80 km s^{-1} range (see Figure 9). Thus, these broad lines are in a turbulent, varying region, possibly located in an outflow.

While the near-IR spectrum of VV CrA is quite complicated, the *Spitzer* IRS spectrum of the VV CrA binary shows only amorphous silicate and CO_2 ice absorption. To determine the optical depths of the silicate and CO_2 ice, we used the broadband fluxes found with the T-ReCS images to estimate continua for the two components. The T-ReCS images indicate almost all of the silicate absorption is toward the IRC, so this feature is not associated with the ISM. To get the optical depth of the silicate and CO_2 ice, we first subtracted the primary continuum from the *Spitzer* IRS spectrum; then we used the same technique used to get the optical depths for DG Tau B. The peak optical depth for the 9.7 μm feature seen toward the IRC is $\tau_{SiO} = 1.35 \pm 0.04$. Using the relation $A_V/\tau_{SiO} = 16.6 \pm 2.1$ from Rieke & Lebofsky (1985) for grains in the ISM, we estimate the extinction to be $A_V = 22.4 \pm 3$ mag, similar to the estimate by Koresko et al. (1997) of 19 mag.

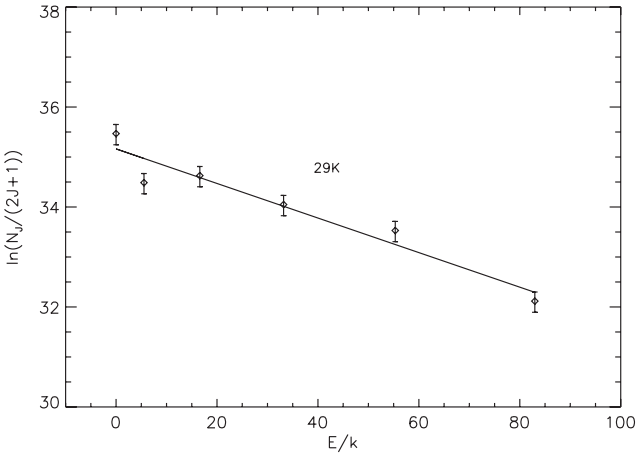

Figure 8. Population diagram of ^{12}CO absorption seen toward the VV CrA primary as measured using CRIRES spectra.

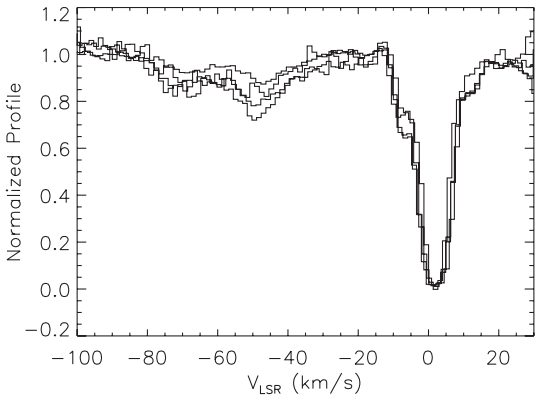

Figure 9. ^{12}CO line profile for the VV CrA IRC found with CRIRES, using the $P(3, 6, 7, 14)$ transitions as examples. The broad absorption found with Phoenix is absent, replaced by other ^{12}CO absorption lines.

For the CO_2 ice feature, if all of the absorption for this feature is associated with the IRC, the optical depth would be $\tau_{CO_2} = 0.055 \pm 0.004$, which would give a ratio $\tau_{SiO}/\tau_{CO_2} = 24.8 \pm 2$. At first glance, this high ratio could imply an edge-on disk geometry when comparing to the Class I YSOs in Taurus (Furlan et al. 2008). However, the τ_{SiO}/τ_{CO_2} ratio found for the IRC is typical of values found by Gibb et al. (2004) for embedded, massive YSOs, and found by Alexander et al. (2003) for low- and intermediate-mass YSOs. Furthermore, the selection in Alexander et al. (2003) included YSOs in the CrA cloud, so an edge-on geometry may not be necessary for the high τ_{SiO}/τ_{CO_2} ratio seen toward the IRC.

4.2. SED Model Fits

We want to characterize the disk structures of DG Tau B and VV CrA in order to have a context for the gas absorption, so we used the online spectral energy distribution (SED) fitting tool described in Robitaille et al. (2006) to get estimates on the disk structure. This tool finds a best fit to an input SED using a database of 200,000 pre-computed radiation transfer models of circumstellar disks, with 14 physical parameters varied at 10 different disk viewing angles. This modeler also estimates the interstellar and circumstellar extinction separately. The user is able to input spectral points, along with the apertures used in the measurements, at wavelengths ranging from the UV to radio. The user can also use upper and lower limits with a

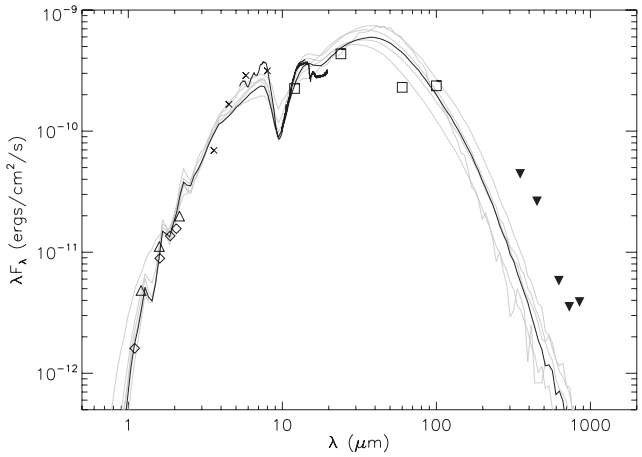

Figure 10. Model fits to the SED of DG Tau B with a best-fit model shown in black and subsequent fits shown in gray. Shown are data from *Spitzer* IRS (continuum), *HST* (diamonds), Two Micron All Sky Survey (triangles), IRAC (crosses; Luhman et al. 2010), *IRAS* (squares; Weaver & Jones 1992), and upper limits (upside-down arrows) from SHARC (Andrews & Williams 2005), SCUBA (Andrews & Williams 2005), and Caltech Submillimeter Observatory (Beckwith & Sargent 1991).

"confidence" percentage that rates how much to penalize models that exceed the limit. The output disk models can be limited to those within a distance and interstellar extinction range. The models are returned in order of increasing χ^2 value, and while a χ^2 cut-off is arbitrary and impossible to make formal when fitting well behaved, symmetric models to less behaved YSOs (Robitaille et al. 2007), we find for our disks that the SED modeler provides good fits up to $\chi^2_{best} - \chi^2 \leqslant 10N$.

While Stark et al. (2006) created synthetic images to model the envelope and disk structure seen in *HST* near-IR images, giving them the advantage of directly modeling images that show disk structure, we can compare and contrast to the model estimates from the SED fitter. This can provide insight into the model results for VV CrA. If we compare the model extinction for VV CrA to our extinction estimates using the optical depth τ_{SiO}, we may be able to constrain the location of the dust, whether in the disk or in the ISM, and test the two disk scenarios presented in S09.

4.2.1. DG Tau B

We constrain the models for DG Tau B to be between 120 and 170 pc away (Gottlieb & Upson 1969; Elias 1978; Kenyon et al. 1994) with interstellar extinction up to $A_V = 15$ mag (Whittet et al. 2001). Our *Spitzer* IRS spectrum was included by inputting the flux at every 1 μm with a 10% error. The SED model fits can be seen in Figure 10, and the parameter results for the best-fit model are listed in Table 7.

The models predict a disk that is not seen edge-on (18°), which is not surprising as Robitaille et al. (2007) found this SED fitting tool does not determine the disk inclination well for most models. Robitaille et al. (2007) used the SED fitting tool to investigate DG Tau B and found an edge-on orientation (inclination = 87°) for those models with no envelope accretion. However, when envelope accretion—as has been found for DG Tau B by Stark et al. (2006)—was added, all inclinations were allowed. We thus exclude disk inclinations from the reported disk parameters.

Stark et al. (2006) modeled DG Tau B with a central star with $M_\star = 0.5\ M_\odot$, $T_\star = 3800$ K, and minimum disk radius 0.03 AU. They calculated an envelope infall rate of $5.0 \times 10^{-6}\ M_\odot\ \mathrm{yr}^{-1}$,

Table 7
Estimated Disk Parameters from SED Fitting of DG Tau B

Parameter	DG Tau B	Literature	Reference
Circumstellar A_V (mag)	36.1 (26.6, 42)	~30	2
Interstellar A_V (mag)	10.5 (6.5, 12.4)		
Stellar temperature (K)	2540 (2540, 2790)	3800[a]	1
Env. infall rate (10^{-6} $M_\odot$ yr^{-1})	1.3 (0.8, 1.8)	2.5[b]	1
Disk accretion rate (10^{-8} $M_\odot$ yr^{-1})	22 (0.4, 48)		
Disk mass (10^{-4} $M_\odot$)	4.4 (1.8, 185)	400	1
Disk inner radius (AU)	0.056 (0.056, 0.44)	0.035[b]	1
Cavity opening angle (°)	3.3 (1.9, 6.2)	30	1

Notes. Shown are the best fit and the (min, max) of the best-fit models.
[a] Used as constants in Stark et al. (2006).
[b] Corrected for model stellar mass, see the text.
References. (1) Stark et al. 2006; (2) Watson et al. 2004.

Table 8
VV CrA Flux Ratios (IRC/Primary) in the Literature

J	*H*	*K*	*L*	*M*	Date Obs.	Reference
1.02	4.66	7.73	10.76		1987 Jun 6–8	Chelli et al. (1995)
		0.515 ± 0.004			1995 Jul 12	Köhler et al. (2008)
0.103	0.299	0.946			1996 Jan 7	Prato et al. (2003)
0.017 ± 0.0001	0.111 ± 0.008	0.358 ± 0.013			2001 Jul 6	Köhler et al. (2008)
0.029		0.34[a]	0.69[a]	0.72[a]	2003 Jul 9	Ratzka et al. (2008)
		0.122 ± 0.006[b]		0.31 ± 0.01[b]	2007 Sep 9	This work: CRIRES
				0.41 ± 0.01[c]	2009 Apr 6	This work: Phoenix

Notes.
[a] The filters used are Ks, L', and M'.
[b] Taken at 2.37 and 4.72 μm.
[c] Taken at 4.62 μm.

which would be $2.2 \times 10^{-6}\,M_\odot\,\mathrm{yr}^{-1}$ after correcting for our model stellar mass of $0.1\,M_\odot$, similar to the SED model prediction of $1.3 \times 10^{-6}\,M_\odot\,\mathrm{yr}^{-1}$. However, the cavity opening angle and disk mass for our models are consistently smaller than those found by Stark et al. (2006).

If we again use the ratio $A_V/\tau_{\mathrm{SiO}} = 16.6 \pm 2.1$ from Rieke & Lebofsky (1985), we can use our measured optical depth $\tau_{\mathrm{SiO}} = 1.52 \pm 0.06$ to estimate the extinction toward DG Tau B to be $A_V = 25.2 \pm 3.3$ mag. Watson et al. (2004) also used this absorption feature to estimate an extinction of 30 mag, which they associate with the circumstellar disk. The best-fit SED model shows a somewhat higher circumstellar extinction of $A_V = 36.1$ mag, but the circumstellar extinction ranges from 26.6 to 42 mag for the disks within the χ^2 cut-off, comparable to our extinction estimate of 25.2 ± 3.3 mag.

While the model results for cavity opening angle and disk mass are small, the other parameters appear to be comparable to previous results and estimates. Although the SED fitter returns circumstellar extinctions that can be higher than previous estimates, the estimates are within the range of those disks in the χ^2 cut-off.

4.2.2. VV CrA

While the IRC dominated the system flux at wavelengths >2.2 μm in the past, it has been progressively fading and is now fainter than the primary at all wavelengths (see Table 8). We can thus only use data taken within a relatively short period of time for modeling the IRC. The primary, on the other hand, has remained constant. Regular observations by the All-Sky Automated Survey (Pojmanski 2002) show the visually dominated primary has a mean $V_{\mathrm{mag}} = 13.8 \pm 0.3$ from the beginning of 2001 through the end of 2009 without any trend.

For the primary fluxes at optical wavelengths, we use the UBVri magnitude ratios reported in Marraco & Rydgren (1981). Reipurth & Zinnecker (1993) could not extract a Gunn z magnitude ratio for VV CrA because the primary was saturated. As the largest ratio they quote is 2%, and because the IRC is even weaker toward optical wavelengths relative to the primary (Koresko et al. 1997), we constrain the IRC flux to be less than 2% of the primary for all wavelengths less than 0.91 μm.

For the near-IR magnitudes of the primary, we use flux values reported by Prato et al. (2003) with observations taken in 1996 and 1997. Again assuming that the primary does not vary, we then use relative ratios found with CRIRES spectra reported in S09 to get a K-band IRC flux. To get far-IR information, we use ISO observations which were taken when the IRC dominated the system flux at those wavelengths. Because the IRC has faded while the primary has remained constant, we use the far-IR magnitudes as upper limits for both the primary and IRC.

For all models of VV CrA, we constrained the distance to be 120–160 pc away (Casey et al. 1998; de Zeeuw et al. 1999). VV CrA has been classified as a late K-type (Appenzeller et al. 1986; Prato et al. 2003), so we also constrained ourselves to those models with stellar temperatures $\lesssim$5,000 K. In order to model the two disk system scenarios proposed by S09, we modeled the IRC twice with two interstellar extinction ranges for the two cases.

For the Case A structure of VV CrA, where the gas absorption is in the primary disk, the primary disk will appear as extinction in the line of sight to the IRC disk rather than in a part of the IRC disk. The SED model fitter uses the KMH model of dust grain sizes described in Kim et al. (1994) to model

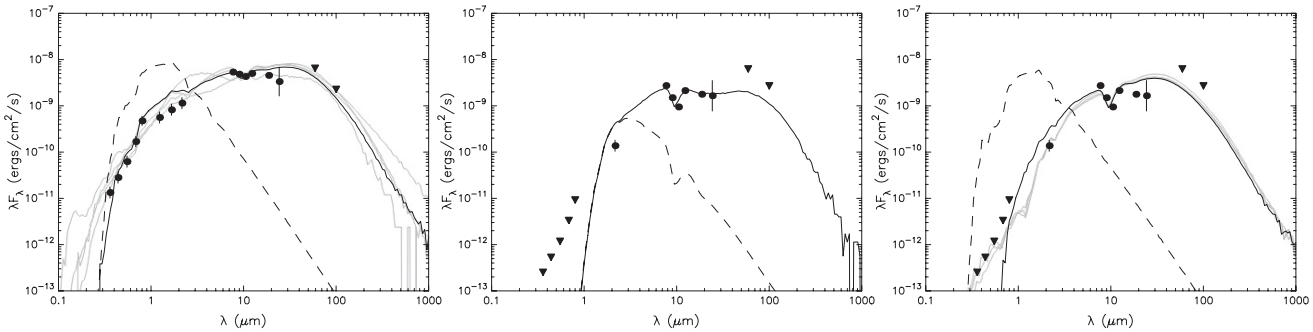

Figure 11. Model fits to SEDs of the VV CrA primary (left) and the VV CrA IRC for two cases: (middle; A) the primary disk is in the line of sight to IRC; (right; B) the IRC disk is the main source of extinction. See the text for a detailed explanation of spectral points (circles) and upper limits (triangles) used. The best-fit model is shown in black and subsequent fits in gray. The dashed line is the stellar photosphere emission for the best-fit model if viewed without circumstellar dust, but including interstellar extinction.

the disk and interstellar extinction, with a modification at wavelengths 1.25–8 μm for the interstellar extinction model (Indebetouw et al. 2005). Because the SED of the IRC is not highly constrained in this wavelength region, we approximate the primary disk as having a grain size distribution similar to the ISM, and thus model it as part of the interstellar extinction up to an estimated 45 mag. For this SED fitting, the number of models returned is very large for our χ^2 cut-off, and hence we lower the cut-off to $\chi^2_{\rm best} - \chi^2 \leqslant 3N$, so that we are not overestimating the parameters (Robitaille et al. 2007). The result for the best fit seen in Figure 11 is given in Table 9. The extinction that we would associate with the primary disk (the interstellar extinction) is 28.6 mag, while the other models within the χ^2 cut-off have a range from 24.3 to 30.2 mag. Our estimate of 22.4 ± 3 mag is at the lower end of the model extinction range, similar to what was found for DG Tau B.

For modeling S09 Case B, if the CO gas is only in the IRC disk, we want to use the interstellar extinction seen toward the primary as an estimate for the IRC, so we first model the primary (see Figure 11). The returned models have interstellar extinction $A_V < 1$ mag, with the best-fit model showing 0 mag. We compare this extinction to the column density measured with the $N(^{12}\mathrm{CO}) = (2.6 \pm 0.4) \times 10^{15}$ cm^{-2} measured toward the primary. The average $N(\mathrm{CO})/A_V = 1.4 \times 10^{17}$ cm^{-2} mag^{-1} for the ISM (Rettig et al. 2006) would suggest a small $A_V \sim 0.02$ mag, showing that this interstellar extinction range is accurate. We therefore constrain the models for the IRC to have an interstellar extinction $A_V < 1$ mag. The resulting best fit seen in Figure 11 has circumstellar extinction of 43.4 mag, and the lowest extinction in the χ^2 cut-off is 35.9 mag, much greater than the estimate of 22.4 ± 3 mag.

Thus, modeling the SED of the IRC for Case A, where the primary disk is the main source of extinction for the IRC, results in extinction estimates that are more consistent with extinction estimates using the optical depth $\tau_{\rm SiO}$, suggesting that this is a more likely scenario.

4.3. Gas and Dust

The gas and dust in disks originate from the surrounding ISM, so if we compare the dust extinction and CO abundance in the disk to the ISM, we can investigate dust settling (Brittain et al. 2005). A change in the dust-to-gas ratio in the line of sight to a central emitting source is largely due to the fact that the two components are not well mixed throughout the disk. Models in Rettig et al. (2006) show that turbulence in the disk will push dust away from the midplane, and the settling velocity increases with grain size due to friction with the gas. This results in a stratification with larger grains closer to the midplane, and more grain growth leads to a higher gas/dust ratio above the midplane. Furthermore, the large gas/dust ratios require grain growth as well as dust settling. We adopt the ratio used by Rettig et al. (2006) $\Delta = [N(\mathrm{CO})/A_V]_{\rm disk}/[N(\mathrm{CO})/A_V]_{\rm interstellar}$, where $[N(\mathrm{CO})/A_V]_{\rm interstellar} = 1.4 \times 10^{17}$ cm^{-2} mag^{-1}. Rettig et al. (2006) probed the gas/dust ratio in the line of sight to the central emitting source of four disks and found that the Δ-ratio ranges from 1.8 for edge-on disks to >8 for face-on disks, and we use these values as a starting point of comparison for DG Tau B and VV CrA.

Rettig et al. (2006) use A_V estimates from *JHK*-band photometry, so the gas and dust are being probed at similar wavelengths. Our extinction estimates are taken from these wavelengths as well as the rest of the SED. However, while the near-IR spectra of DG Tau B and VV CrA primary are well constrained, this is not the case for the VV CrA IRC. Thus, this should be taken as a first estimate for the IRC.

4.3.1. DG Tau B

We use our ^{12}CO column density of $(2.42 \pm 0.04) \times 10^{19}$ cm^{-2} and circumstellar extinction, estimated using the $\tau_{\rm SiO}$, of 25.2 ± 3.3 mag to find $\Delta = 6.86 \pm 0.9$. This is significantly larger than the ratios found toward other edge-on disks in Rettig et al. (2006), which were ~1.8. If we use the extinction found with the SED modeling, 36.1 mag, the Δ-ratio would still be 4.8. Furthermore, we are using the column density estimated from the ^{13}CO column density and the mean local ISM isotopic ratio (Wilson 1999). If the ^{12}CO is self-shielding, as was found in the disks in S09, the $N(^{12}\mathrm{CO})/N(^{13}\mathrm{CO})$ would increase from the ISM, and the Δ-ratio would only be larger. This indicates a larger grain growth and settling in DG Tau B than seen toward the disks in Rettig et al. (2006).

For comparison, Lahuis et al. (2006) found $\tau_{\rm SiO} = 0.86$ ($A_V = 16.6\tau_{\rm SiO} = 14.2$ mag) and $N(\mathrm{CO}) = 2 \times 10^{18}$ cm^{-2}, giving $\Delta = 1.0$ for IRS 46. For GV Tau N, Bowey & Adamson (2001) found $\tau_{\rm SiO} = 1.7$ and Gibb et al. (2007) found $N(\mathrm{CO}) = 5.9 \times 10^{18}$ cm^{-1}, giving $\Delta = 1.5$. IRS 46 and GV Tau N thus have gas/dust ratios more similar to the ISM, as expected for edge-on disks, further emphasizing the high Δ-ratio found in DG Tau B. This also suggests that the line of sight in DG Tau B is not probing deeper in the disk atmosphere than the lines of sight for IRS 46 and GV Tau N, nearer where the dust is settled, as is suggested by the $\tau_{\rm SiO}/\tau_{\rm CO_2}$ ratio. Rather, the higher $\tau_{\rm SiO}/\tau_{\rm CO_2}$ ratios in IRS 46 and GV Tau N may just be due to having lines of sight that view more silicate in the warmer regions of the disk, where the CO_2 ice has sublimated, than for DG Tau B.

Table 9
Estimated Disk Parameters from SED Fitting of the VV CrA Primary and for the IRC for Cases A and B

Parameter	Primary	IRC: Case A	IRC: Case B
Circumstellar A_V (mag)	26.0 (20, 31)	0.15 (0.0003, 0.15)	43.4 (36, 43.4)
Interstellar A_V (mag)	0 (0, 1.0)	28.6 (24.4, 30)	0 (0, 1.0)
Stellar temperature (K)	3560 (3440, 3650)	5180 (5070, 5410)	3380 (3240, 3380)
Env. infall rate (10^{-6} $M_\odot$ yr^{-1})	3.5 (2.5, 6.3)	0.02 (0, 0.02)	2.1(1.7, 2.1)
Disk accretion rate (10^{-8} $M_\odot$ yr^{-1})	6.7 (6.7, 200)	4.1 (4.1, 6.1)	4.1 (4.1, 150)
Disk mass (10^{-3} $M_\odot$)	1.5 (1.1, 7.3)	26.7 (4.4, 80)	7.5 (7.0, 7.5)
Disk inner radius (AU)	0.2 (0.15, 8.0)	3.5 (2.2, 3.5)	0.1 (0.1, 1.3)
Cavity opening angle (°)	5.9 (2.9, 7.7)	55.5 (32, 55.5)	1.4 (1.4, 2.0)

Note. Shown are the best fit and the (min, max) of the best-fit models.

4.3.2. VV CrA

The Δ ratios in Rettig et al. (2006) are for probing the gas/dust ratio in the radial structure toward the central emitting source. This method can therefore not be used to test the Case A structure for VV CrA, as the geometry in this scenario would be probing the vertical structure of the primary disk. For Case B, the VV CrA IRC was found by S09 to have a hot ^{12}CO gas component with the column density of $7.15 \pm 0.17 \times 10^{18}$ cm^{-2} and cold ^{12}CO gas component with column density $> (1.40 \pm 0.07) \times 10^{18}$ cm^{-2}. By adding these column densities, and using the A_V estimate of 22.4 ± 3 found with the silicate absorption, we find $\Delta \geqslant 2.74$. Comparing to the other sources in Rettig et al. (2006), this is comparable to a disk with inclination $\sim 60°$.

4.4. Velocity Shift in DG Tau B

The warm gases toward IRS 46 and GV Tau N show velocity shifts that suggest they are not in simple Keplerian rotation in the disk. IRS 46 shows ^{12}CO and HCN blueshifted ~ 24 km s^{-1} from the quiescent cloud (Lahuis et al. 2006), and GV Tau N shows warm HCN redshifted ~ 13 km s^{-1} from the stellar velocity (Doppmann et al. 2008). Similarly, DG Tau B shows a shift that raises the question of where the gas resides.

The molecular cloud surrounding DG Tau B has a velocity $V_{\rm LSR} = 6.5$ km s^{-1} (Mitchell et al. 1994), so we would expect a similar velocity for DG Tau B (Herbig 1977). However, the ^{13}CO and high-J ^{12}CO gas seen toward DG Tau B have an excess redshift of $\sim$6–7 km s^{-1}, so the gas does not appear to be in simple Keplerian rotation. The gas is not likely associated with a disk wind, which would result in a blueshift, or with the optical jets as they have velocities >50 km s^{-1} and <-90 km s^{-1} relative to the cloud velocity (Eislöffel & Mundt 1998). A molecular outflow was found to have blue ($V_{\rm LSR}$ = from -3.8 to 5.1 km s^{-1}) and red (from 7.5 to 10.9 km s^{-1}; Mitchell et al. 1997) components, but our observed shift is outside these bounds. While the CO velocity shift is near the extreme end of the red outflow, *JHK*-band images show that the main source of continuum is southeast of the dark lane (Padgett et al. 1999), in the direction of the blue outflow component. The molecular outflow does encase the surrounding cloud velocity, indicating that the DG Tau B systemic velocity is likely similar to the surrounding cloud.

One explanation for the observed shift could be infalling gas. Assuming the stellar mass of 0.1 $M_\odot$ from our SED model fitting, the velocity of the infalling gas $V_r = (2GM_\star/r)^{1/2}$ would be 6 km s^{-1} at $r = 5$ AU. An envelope infall rate of 1.3×10^{-6} $M_\odot$ yr^{-1} would imply a density $n_{\rm H} = \dot{M}/(2\pi r^2 {\rm v} m_{\rm H}) = 2.3 \times 10^9$ cm^{-3}. Assuming a CO/H ratio of $\sim 3 \times 10^{-4}$ and a column length of 5 AU, we would estimate a column density of 5×10^{19} cm^{-2}, similar to our measured 2.4×10^{19} cm^{-2}. At this radius, the accretion radiation from an infalling envelope has been modeled to heat the gas to $\sim$300 K for $L \geqslant 20$ $L_\odot$ (see Figure 4 in Ceccarelli et al. 1996). However, the total luminosity of DG Tau B is quite small compared to those models, found previously to range between 0.2 and 2.5 $L_\odot$ (Stark et al. 2006; Furlan et al. 2008), and between 0.7 and 1.5 $L_\odot$ by our SED model fits. If we were to increase the stellar mass to 0.5 $M_\odot$, this would push a 6 km s^{-1} infall out to 25 AU, where even an accretion radiation of 65 $L_\odot$ would result in gas temperatures $<$200 K. Also, if the CO gas is associated with an infalling envelope, we would expect the gas/dust ratio to be near the ISM value, contrary to our findings. The absorption is thus unlikely to be associated with an infalling envelope.

Another possible explanation for the observed velocity shift could be that the CO is in the disk of a non-axisymmetric system. The main M-band continuum source is likely the disk which could be non-axisymmetric, possibly due to having a close stellar or planetary companion, hot spots in the disk, or some similar phenomenon. Also, the absorbing gas may be non-axisymmetric, as would be the case for an asymmetric disk atmosphere. In either case, the absorption would vary in velocity, but average out over time to the systemic velocity. Although observations that show such a velocity variation would be needed to support this hypothesis, it currently appears to be the most likely scenario.

4.5. Conclusion

While the *Spitzer* IRS was an excellent instrument to detect molecular signatures in circumstellar disks, the detection of organic molecules in absorption was rare. DG Tau B is one disk that showed molecular gas in absorption. While we were able to directly detect CO_2, we only found upper limits for C_2H_2 and HCN, the other species found toward IRS 46 with the *Spitzer* IRS (Lahuis et al. 2006). This could simply be a function of lower gas abundances in the disk, or this could be due to probing a slightly different region of the disk where C_2H_2 and HCN have lower abundances, as is suggested by the gas column densities and gas/ice ratios. Although we are viewing an edge-on disk like IRS 46 and GV Tau N, this could imply that molecular absorption is highly sensitive to even moderate changes in the line of sight in the disk, which may account for the rarity of such detections even in edge-on disks. Furthermore, the large CO column density to extinction ratio indicates the disk is likely showing a large amount of grain growth and dust settling when compared to other disks (Rettig et al. 2006). Finally, while the velocity shift of the absorbing CO gas is difficult to explain, the most likely scenario currently appears to be that the CO is

in the disk while the main continuum emitting source or the absorbing gas is non-axisymmetric.

While the *Spitzer* IRS spectrum of VV CrA shows only silicate and CO_2 ice absorption, high-resolution spectroscopy reveals that the disk has a complicated and changing near-IR spectrum. Smith et al. (2009) proposed the absorbing CO gas seen toward the IRC is located (A) within the primary disk in the line of sight to the IRC, or (B) within the disk around the IRC. To test these cases, we used T-ReCS images to separate the fluxes of the VV CrA components in the IRS spectrum, allowing us to determine a dust extinction estimate for the IRC. We then modeled the SED for the IRC with two interstellar extinction ranges, simulating the two cases proposed by S09, and found that the disk models for Case A return circumstellar extinction magnitudes more consistent with our extinction estimate. This supports the view by Smith et al. (2009) that this is a more likely case.

We would like to thank Thomas Robitaille, Thorsten Ratzka, John Lacy, and the anonymous reviewer for their constructive help, comments, and suggestions. Support for this work was provided by the National Science Foundation under grant No. AST-0708074, and by NASA through contract RSA No. 1346810, issued by JPL/Caltech. This work is based on observations made with the *Spitzer Space Telescope*, Gemini Observatory, and W.M. Keck Observatory. The *Spitzer Space Telescope* is operated by the Jet Propulsion Laboratory, California Institute of Technology under a contract with NASA. The Gemini Observatory is operated by the Association of Universities for Research in Astronomy, Inc., under a cooperative agreement with the NSF on behalf of the Gemini partnership: the National Science Foundation (United States), the Science and Technology Facilities Council (United Kingdom), the National Research Council (Canada), CONICYT (Chile), the Australian Research Council (Australia), Ministério da Ciência e Tecnologia (Brazil), and Ministerio de Ciencia, Tecnología e Innovación Productiva (Argentina). The W.M. Keck Observatory is operated as a scientific partnership among the California Institute of Technology, the University of California, and the National Aeronautics and Space Administration. The Observatory was made possible by the generous financial support of the W.M. Keck Foundation. Basic research in infrared astronomy at the Naval Research Laboratory is supported by 6.1 base funding.

REFERENCES

Agúndez, M., Cernicharo, J., & Goicoechea, J. R. 2008, A&A, 483, 831
Alexander, R. D., Casali, M. M., André, P., Persi, P., & Eiroa, C. 2003, A&A, 401, 613
Andrews, S. M., & Williams, J. P. 2005, ApJ, 631, 1134
Appenzeller, I., Jankovics, I., & Jetter, R. 1986, A&AS, 64, 65
Beckwith, S. V. W., & Sargent, A. I. 1991, ApJ, 381, 250
Bergin, E. A., Aikawa, Y., Blake, G. A., & van Dishoeck, E. F. 2007, in Protostars and Planets V, ed. B. Reipurth, D. Jewitt, & K. Keil (Tucson, AZ: Univ. Arizona Press), 751
Bowey, J. E., & Adamson, A. J. 2001, MNRAS, 320, 131
Brittain, S. D., Rettig, T. W., Simon, T., & Kulesa, C. 2005, ApJ, 626, 283
Brittain, S. D., Simon, T., Najita, J. R., & Rettig, T. W. 2007, ApJ, 659, 685
Carr, J. S., & Najita, J. R. 2008, Science, 319, 1504
Casey, B. W., Mathieu, R. D., Vaz, L. P. R., Anderson, J., & Suntze, N. B. 1998, AJ, 115, 1617
Ceccarelli, C., Hollenbach, D. J., & Tielens, A. G. G. M. 1996, ApJ, 471, 400
Chelli, A., Cruz-Gonzalez, I., & Reipurth, B. 1995, A&A, 114, 135
Correia, S., Ratzka, T., Duchene, G., & Zinnecker, H. 2007, in IAU Symp. 240, Binary Stars as Critical Tools and Tests in Contemporary Astrophysics, ed. W. I. Hartkopf, E. F. Guinan, & P. Harmanec (Cambridge: Cambridge Univ. Press), 213
de Zeeuw, P. T., Hoogerwerf, R., de Bruijne, J. H. J., Brown, A. G. A., & Blaauw, A. 1999, AJ, 117, 354
Doppmann, G. W., Najita, J. R., & Carr, J. S. 2008, ApJ, 685, 298
Eislöffel, J., & Mundt, R. 1998, AJ, 115, 1554
Elias, J. H. 1978, ApJ, 224, 857
Evans, N. J., et al. 2003, PASP, 115, 965
Furlan, E., et al. 2008, ApJS, 176, 184
Gibb, E. L., Van Brunt, K. A., Brittain, S. D., & Rettig, T. W. 2007, ApJ, 660, 1572
Gibb, E. L., Whittet, D. C. B., Boogert, A. C. A., & Tielens, A. G. G. M. 2004, ApJS, 151, 35
Glassgold, A. E., Meijerink, R., & Najita, J. R. 2009, ApJ, 701, 142
Glassgold, A. E., Najita, J. R., & Igea, J. 2007, ApJ, 656, 515
Gottlieb, D. M., & Upson, W. L. 1969, ApJ, 157, 611
Güdel, M., et al. 2010, A&A, 519, A113
Herbig, G. H. 1977, ApJ, 214, 747
Hinkle, K. H., Cuberly, R. W., Gaughan, N. A., Heynssens, J. B., Joyce, R. R., Ridgway, S. T., Schmitt, P., & Simmons, J. E. 1998, Proc. SPIE, 3354, 810
Hollenbach, D., & Gorti, U. 2009, ApJ, 703, 1203
Houck, J., et al. 2004, ApJS, 154, 18
Indebetouw, R., et al. 2005, ApJ, 619, 931
Kenyon, S. J., Dobrzycka, D., & Hartmann, L. 1994, AJ, 108, 1872
Köhler, R., Neuhäuser, R., Krämer, S., Leinert, Ch., Ott, T., & Eckart, A. 2008, A&A, 488, 997
Kim, S. H., Martin, P. G., & Hendry, P. D. 1994, ApJ, 422, 164
Koresko, C. D., Herbst, T. M., & Leinert, Ch. 1997, ApJ, 480, 741
Lahuis, F., van Dishoeck, E. F., Blake, G. A., Evans, N. J., II, Kessler-Silacci, J. E., & Pontoppidan, K. M. 2007, ApJ, 665, 492
Lahuis, F., et al. 2006, ApJ, 636, L145
Luhman, K. L., Allen, P. R., Espaillat, C., Hartmann, L., & Calvet, N. 2010, ApJS, 167, 256
Markwick, A. J., Ilgner, M., Millar, T. J., & Henning, Th. 2002, A&A, 385, 632
Marraco, H. G., & Rydgren, A. E. 1981, AJ, 86, 62
McLean, I. S., et al. 1998, Proc. SPIE, 3354, 566
Mitchell, G. F., Hasegawa, T. I., Dent, W. R. F., & Matthews, H. E. 1994, ApJ, 436, L177
Mitchell, G. F., Sargent, A. I., & Mannings, V. 1997, ApJ, 483, L127
Mundt, R., & Fried, J. W. 1983, ApJ, 274, L83
Najita, J., Carr, J. S., & Mathieu, R. D. 2003, ApJ, 589, 931
Padgett, D. L., Brandner, W., Stapelfeldt, K. R., Strom, S. E., Tereby, S., & Koerner, D. 1999, AJ, 117, 1490
Pojmanski, G. 2002, Acta Astron., 52, 397
Pontoppidan, K. M., Salyk, C., Blake, G. A., Meijerink, R., Carr, J. S., & Najita, J. 2010, ApJ, 720, 887
Pontoppidan, K. M., et al. 2008, ApJ, 678, 1005
Prato, L., Greene, T. P., & Simon, M. 2003, ApJ, 584, 853
Ratzka, Th., Leinert, Ch., Przygodda, F., & Wolf, S. 2008, in The Power of Optical/IR Interferometry: Recent Scientific Results and 2nd Generation Instrumentation, ed. A. Richichi, F. Delplancke, F. Paresce, & A. Chelli, 431
Reipurth, B., & Zinnecker, H. 1993, A&A, 278, 81
Rettig, T., Brittain, S., Simon, T., Gibb, E., Balsara, D. S., Tilley, D. A., & Kulesa, C. 2006, ApJ, 646, 342
Rieke, G. H., & Lebofsky, M. J. 1985, ApJ, 288, 618
Robitaille, T. P., Whitney, B. A., Indebetouw, R., & Wood, K. 2007, ApJS, 169, 328
Robitaille, T. P., Whitney, B. A., Indebetouw, R., Wood, K., & Denzmore, P. 2006, ApJS, 167, 256
Rothman, L. S., et al. 1998, J. Quant. Spectrosc. Radiat. Transfer, 60, 665
Salyk, C., Pontoppidan, K. M., Blake, G. A., Lahuis, F., van Dishoeck, E. F., & Evans, N. J., II. 2008, ApJ, 676, L49
Seifahrt, A., Käufl, H. U., Zängl, G., Bean, J. L., Richter, M. J., & Siebenmorgen, R. 2010, A&A, 524, A11
Smith, R. L., Pontoppidan, K. M., Young, E. D., Morris, M. R., & van Dishoeck, E. F. 2009, ApJ, 701, 163
Stapelfeldt, K., Burrows, C. J., & Krist, J. E. the WFPC2 Science Team. 1997, in IAU Symp. 182, Herbig–Haro Flows and the Birth of Stars, ed. B. Reipurth & C. Bertout (Dordrecht: Kluwer Academic Publishers), 355
Stark, D. P., Whitney, B. A., Stassun, K., & Wood, K. 2006, ApJ, 649, 900
Telesco, C. M., Pina, R. K., Hanna, K. T., Julian, J. A., Hon, D. B., & Kisko, T. M. 1998, Proc. SPIE, 3354, 534
Watson, D. M., et al. 2004, ApJS, 154, 391
Weaver, W. B., & Jones, G. 1992, ApJS, 78, 239
Whittet, D. C. B., Gerakines, P. A., Hough, J. H., & Shenoy, S. S. 2001, ApJ, 547, 872
Wilson, T. L. 1999, Rep. Prog. Phys., 62, 143
Woods, P. M., & Willacy, K. 2009, ApJ, 693, 1360
Zasowski, G., Kemper, F., Watson, D. M., Furlan, E., Bohac, C. J., Hull, C., & Green, J. D. 2009, ApJ, 694, 459